ACS OMEGA

http://pubs.acs.org/journal/acsodf

Article

Effects of Sonication and Hydrothermal Treatments on the Optical and Chemical Properties of Carbon Dots

I-Hua Tsai, Jyun-Ting Li, and Chih-Wei Chang*

Cite This: *ACS Omega* 2021, 6, 14174−14181

Read Online

ACCESS | Metrics & More | Article Recommendations | Supporting Information

ABSTRACT: In our study, we have tested the effects of sonication and hydrothermal treatments on the properties of carbon dots synthesized from a microwave-assisted method (C-dots^{MW}). When the carbon dots are sonicated in an aerobic environment, the fluorescence quantum yield decreases drastically because the molecular fluorophores attached to the surface of the carbon dots are oxidized during the sonication process. Meanwhile, the sonicated C-dots^{MW} also lose their Hg^{2+} ion sensing and photoreduction activity due to the oxidization of surface functional groups. After the hydrothermal treatment, the fluorescence quantum yield of C-dots^{MW} increases due to the formation of new fluorophores; however, the Hg^{2+} ion sensitivity and photoreduction activity of C-dots^{MW} decrease significantly due to the oxidization of surface functional groups. By autoclaving the C-dots^{MW} at 100 °C, we have demonstrated that we can enhance the fluorescence quantum yield of C-dots^{MW} without losing their Hg^{2+} ion sensitivity. This finding can be used to improve the fluorescence quantum yield of the fluorescent ion sensor based on C-dots.

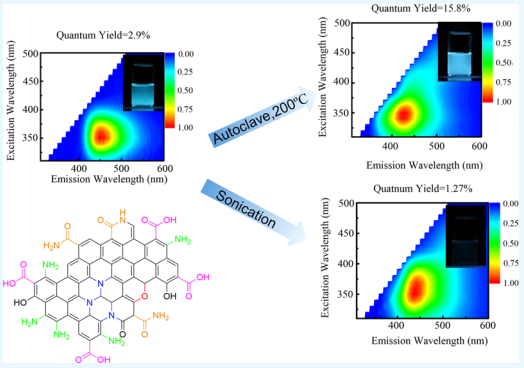

INTRODUCTION

Carbon dots (C-dots), since their discovery in 2004,[1] have received particular attention because of their versatile optical and chemical properties that can be utilized in different fields including sensing,[2−5] optical imaging,[6−11] catalysis,[12−15] and light-emitting devices.[16−18] The term C-dots indicate the nanosized carbon materials (<10 nm) that consist of sp^2/sp^3 carbon skeletons and oxygen/nitrogen functional groups on their surface.[19,20] In contrast to inorganic nanoparticles, C-dots are highly soluble in water and exhibit low toxicity, and[21] hence, they have been extensively applied in bioimaging and phototherapy studies.[22−24] The recent studies indicated that the properties of C-dots can be tuned by incorporating C-dots with other molecules or nanomaterials. For example, Xu et al. have reported that modifying the amino-functional groups on the surface of C-dots could significantly increase the photocatalytic hydrogen generation efficiency of C-dots.[25] The glutathione-modified C-dots exhibit aggregation-induced emission and have been utilized as a turn-on fluorescence sensor for Fe^{3+} ions.[4] When the N-doped C-dots were decorated on TiO_2 nanoparticles (P25), the P25/N-doped C-dot composite showed enhanced NO photooxidation activities.[13] C-dots can also be used to enhance the photocatalytic activities of Bi_2WO_6.[26] Several studies indicated that when C-dots were encapsulated in zeolites, the C-dots/zeolite nanocomposite exhibited thermally activated delayed fluorescence emission.[27−30]

Because most applications of C-dots rely on their optical properties, understanding the emission origin and controlling the optical properties of C-dots have become some of the most challenging tasks in this field. The UV−vis absorption spectra of C-dots were featured by the absorption bands originated from the $\pi-\pi^*$ transition of aromatic rings and the $n-\pi^*$ transition of the C═O bond.[19] Recent studies indicate that the emission properties of C-dots are highly dependent on their size[31] and types of surface functional groups.[19,32] For the C-dots prepared from citric acid (CA) and amines, pyrolysis generates various highly emissive 2-pyridone derivatives, while the fluorophore forms a carbogenic core as the pyrolysis proceeds.[33−36] It is generally believed that 2-pyridone derivatives are attached on the surface of C-dots. However, Das et al. showed that for the C-dots derived from CA and ethanolamine, some of the highly emissive fluorophores were trapped in the flexible region inside the C-dots.[37] In the bottom-up approach, the hydrothermal and microwave methods are two of the most popular methods for synthesizing the C-dots. For the C-dots prepared by the hydrothermal method, the entire reaction includes the following steps: (1) the starting materials (CA with various amine derivatives) form molecular fluorophore- and polymer-aggregated nanoparticles;

Received: February 10, 2021
Accepted: May 12, 2021
Published: May 24, 2021

(2) the polymer aggregates are carbonized to form a carbon core and the molecular fluorophores are further reacted and attached on the surface of carbon dots; and (3) the molecular fluorophores are further carbonized, and the emission of C-dots drops because of the loss of molecular fluorophores.[38−40] Since the mechanism was deduced by analyzing the C-dots prepared at different hydrothermal temperatures, the detailed formation mechanism for the C-dots obtained from a domestic microwave oven is unclear. The reaction temperature and pressure in the domestic microwave oven are significantly lower than those in a hydrothermal container; therefore, it is reasonable for us to expect that the C-dots obtained from the microwave method (C-dots^{MW}) are still at the initial stage of pyrolysis or the carbonization process, and their optical or chemical properties could be improved by further reactions. To address this point, we have prepared C-dots^{MW} from CA + ethylenediamine, and they were further treated by sonication or hydrothermal methods. After sonication and hydrothermal treatments, the optical properties, particle sizes, surface functional groups, Hg^{2+} ion-sensing capability, and photoreduction activities of the post-treated C-dots^{MW} were compared with C-dots^{MW}. The information we provided can help us to elucidate the origin of the ion sensing and photoreduction abilities of C-dots and the details are discussed in the following paragraphs.

RESULTS AND DISCUSSION

Effects of Sonication on the Optical Properties of C-Dots^{MW}. Figure 1a shows the steady-state absorption and emission spectra of C-dots^{MW} and C-dots^{MW} sonicated in an ultrasonic bath (E30H, Elma) for 2 h (C-dots$^{MW}_{sonicated}$). The absorption spectrum of C-dots^{MW} was featured by $\pi \rightarrow \pi^*$ and $n \rightarrow \pi^*$ transition bands centered at 245 and 355 nm, respectively. Upon 350 nm excitation, C-dots^{MW} showed an emission band centered at 450 nm, while the fluorescence quantum yield (Φ_f) was estimated to be 2.90%. In contrast to C-dots^{MW}, the absorption and emission spectra of C-dots$^{MW}_{sonicated}$ are blue-shifted, while Φ_f drops to 1.27%. In the transmission electron microscopy (TEM) images (Figure S1), the size distribution of C-dots$^{MW}_{sonicated}$ is slightly larger than that of C-dots^{MW}; therefore, the hypsochromic shifts of the steady-state spectra cannot be associated with the quantum confinement effect.

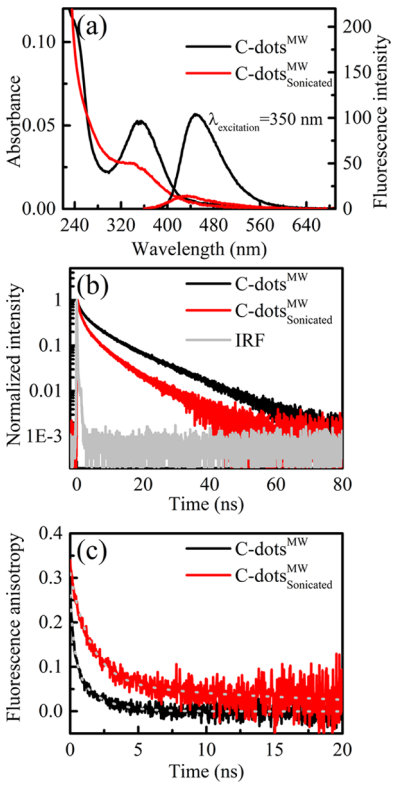

Figure 1. (a) Steady-state spectra, (b) fluorescence decay, and (c) fluorescence anisotropy decay dynamics of C-dots^{MW} and C-dots$^{MW}_{sonicated}$. The dashed line indicates the fitting curve of the fluorescence anisotropy decay dynamics. The excitation wavelength was fixed at 375 nm.

In the excitation wavelength between 320 and 400 nm (Figure S2), the emission peaks of C-dots^{MW} are independent of the excitation wavelength, while C-dots$^{MW}_{sonicated}$ show clear excitation-dependent fluorescence (EDF) in this range. Because the emission originated from the carbon core usually exhibits low Φ_f and EDF, the results indicated that the fluorescence of C-dots^{MW} was originated from molecule-like fluorophores. After sonication, the molecule-like fluorophores are consumed, hence the emission originated from the carbon core becomes important in C-dots$^{MW}_{sonicated}$. Figure 1b illustrates the fluorescence decay dynamics of C-dots^{MW} and C-dots$^{MW}_{sonicated}$, and the fitting parameters are summarized in Table 1. The analysis shows that the averaged fluorescence lifetime ($\tau_{average}$) decreases from 10.44 ns for C-dots^{MW} to 5.33 ns for C-dots$^{MW}_{sonicated}$. Thus, the radiative lifetime ($\tau_{radiative}$) can be estimated using the following equation

$$\Phi = \frac{\tau_{average}}{\tau_{radiative}} = \frac{k_r}{k_r + k_{nr}} \quad (1)$$

where k_r and k_{nr} indicate the rate constants of the radiative and nonradiative processes, respectively. Since C-dots^{MW} and C-dots$^{MW}_{sonicated}$ exhibit similar k_r, the lower Φ_f of C-dots$^{MW}_{sonicated}$ is due to the higher k_{nr} of the carbon core. Figure 1c illustrates the fluorescence anisotropy decay dynamics, $r(t)$, of C-dots^{MW} and C-dots$^{MW}_{sonicated}$. The $r(t)$ can be fitted by the following biexponential model

$$r(t) = a_1 e^{-t/\tau_1} + a_2 e^{-t/\tau_2} \quad (2)$$

where τ_1 and τ_2 indicate the fast and slow time coefficients, respectively. For molecular fluorophores attached to the carbon core, τ_1 and τ_2 can be represented by the correlation time of segmental motions (τ_s) and the rotation of entire C-dots (τ_r)[41]

$$\frac{1}{\tau_1} = \frac{1}{\tau_s} + \frac{1}{\tau_r}, \frac{1}{\tau_2} = \frac{1}{\tau_r} \quad (3)$$

The hydrodynamic radius, r_H, of C-dots can be estimated from the Stocks−Einstein−Debye equation

$$r_H = \sqrt[3]{\frac{3k_B T\tau_2}{4\pi\eta}} \quad (4)$$

where k_B is the Boltzmann constant, T is the temperature, and η is the viscosity of the solvent. According to the anisotropy data (Table 2), the r_H values of C-dots^{MW} and C-dots$^{MW}_{sonicated}$ were estimated to be 1.3 and 2.9 nm, respectively. Our analysis also shows that τ_s slows down after sonication. The result suggested that C-dots^{MW} lost their flexible molecule-like

https://doi.org/10.1021/acsomega.1c00765
ACS Omega 2021, 6, 14174−14181

Table 1. Fluorescence Quantum Yield and the Fitting Parameters for the Fluorescence Decay Dynamics[c]

		C-dots^{MW}	C-dots$^{MW}_{sonicated}$	C-dots$^{MW}_{100°C}$	C-dots$^{MW}_{200°C}$
fluorescence quantum yield (Φ_f)[a]	2.90%	1.27%	8.70%	15.8%	
[b]fluorescence decay[b]	τ_1 (a_1)	0.46 ns (0.51)	0.24 ns (0.68)	0.41 ns (0.43)	0.62 ns(0.45)
	τ_2 (a_2)	3.77 ns (0.29)	1.86 ns(0.25)	3.57 ns (0.29)	3.22 ns (0.45)
	τ_3 (a_3)	13.9 ns (0.20)	9.15 ns (0.07)	14.0 ns (0.28)	10.2 ns (0.10)
	$\tau_{average}$	10.4 ns	5.33 ns	11.43 ns	5.72 ns
	k_r	2.78×10^6 s^{-1}	2.38×10^6 s^{-1}	7.61×10^6 s^{-1}	2.76×10^7 s^{-1}
	k_{nr}	9.30×10^7 s^{-1}	1.85×10^8 s^{-1}	7.99×10^7 s^{-1}	1.47×10^8 s^{-1}

[a]Estimated using a solution of quinine sulfate and 0.1 M H_2SO_4 as a reference. [b]The kinetic model used for deconvolution is $I(t) = a_1e^{-t/\tau_1} + a_2e^{-t/\tau_2} + a_3e^{-t/\tau_3}$. [c]$\tau_{average} = \frac{a_1\tau_1^2 + a_2\tau_2^2 + a_3\tau_3^2}{a_1\tau_1 + a_2\tau_2 + a_3\tau_3}$.

Table 2. Fitting Parameters of the Fluorescence Anisotropy Decay Dynamics and the Radius Estimated by Different Methods

		C-dots^{MW}	C-dots$^{MW}_{sonicated}$	C-dots$^{MW}_{100°C}$	C-dots$^{MW}_{200°C}$
fluorescence anisotropy[a]	τ_1 (a_1)	0.32 ns(0.16)	1.57 ns (0.25)	0.31 ns (0.17)	
	τ_2 (a_2)	1.82 ns (0.10)	22.5 ns (0.06)	1.91 ns (0.06)	0.20 ns (0.22)
	τ_s	0.39 ns	1.68 ns	0.37 ns	
hydrodynamic radius estimated by τ_2[b]		1.3 nm	2.9 nm	1.3 nm	0.7 nm
radius estimated by TEM		1.2 nm	1.5 nm	1.0 nm	0.9 nm

[a]Fluorescence anisotropy, $r(t) = a_1 \times e^{-t/\tau 1} + a_2 \times e^{-t/\tau 2}$. [b]$T$ = 298 K and η = 0.89 cP.

fluorophores and only the carbon core or the chromophores buried in a more restricted environment can survive after sonication.

Structural Characterization of C-Dots, and the Changes in the Chemical Properties of C-Dots^{MW} after Sonication. To further identify the changes in surface functional groups after sonication, we also compared the Fourier transform infrared (FT-IR) spectra and X-ray photoelectron spectra (XPS) of C-dots. From the FT-IR spectrum of C-dots^{MW} (Figure 2a), we found the characteristics peaks of −OH and −NH (I: ∼3400 and 3300 cm^{-1}, respectively), C−H stretching (II: 3085 and 2940 cm^{-1}),[42] C═O for the carboxylic acid monomer and dimer (III: 1774/1700 cm^{-1}),[43] amide vibrational modes I and II (IV: 1650 and 1555 cm^{-1}, respectively),[43] amine N−H (V: 1434 cm^{-1}),[42] C−OH from either alcohols or carboxylic groups (VI: 1403 and 1357 cm^{-1}, respectively), epoxy C−O−C (VII: 1236 and 1187 cm^{-1}),[44,45] and alkoxy C−O (VIII: 1025 cm^{-1})[44] functional groups. The FT-IR spectrum of C-dots$^{MW}_{sonicated}$ (Figure 2b) is distinct from that of C-dots^{MW} in two aspects. First, the relative intensity of the vibrational band at 1774 and 1434 cm^{-1} of C-dots$^{MW}_{sonicated}$ is lower than that of C-dots^{MW}, which indicates the loss of carboxylic acid and −NH functional groups. Second, C-dots$^{MW}_{sonicated}$ show an additional band that corresponds to the vibration of alkoxy C−O groups at ∼1025 cm^{-1}. The result implies that C-dots^{MW} are oxidized upon sonication. The interpretation is also supported by the XPS spectra. In the XPS survey spectra (Figure 2c), the atomic percent composition of carbon/nitrogen/oxygen changes from 62:15:23 for C-dots^{MW} to 64:4:32 for C-dots$^{MW}_{sonicated}$. The C 1s high-resolution XPS spectra of C-dots^{MW} (Figure 2d) shows six peaks, which indicates the presence of C═C[46] or carbon defects[47] (α: 283.6 eV), C−C/C═C (β: 284.8 eV), C−OH (γ: 285.7 eV), C−O−C (δ: 286.7 eV), N−C═O (ε: 287.5 eV), and HO−C═O (ζ: 288.2 eV) bonds.[13,43,48] In the C 1s spectra of C-dots$^{MW}_{sonicated}$ (Figure 2e), the signal corresponding to the carbon core region (α and β) increases, while the signal corresponding to the

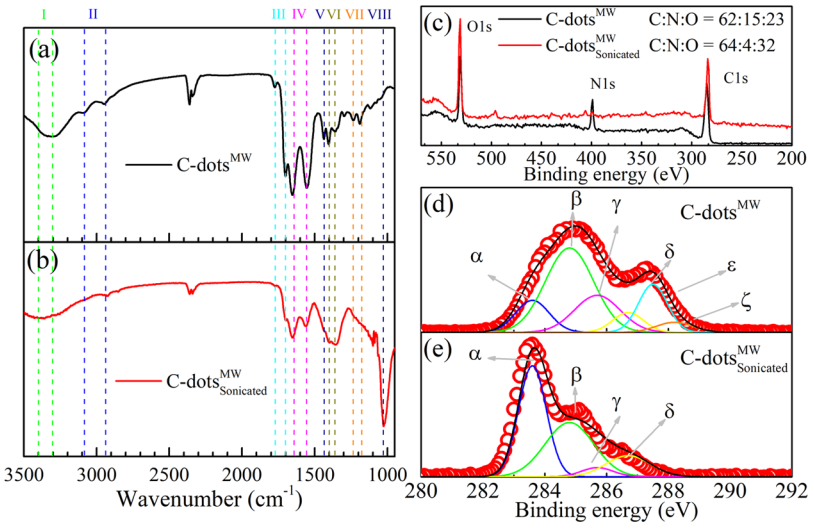

Figure 2. FT-IR spectra of (a) C-dots^{MW} and (b) C-dots$^{MW}_{sonicated}$; (c) the XPS survey scan of C-dots^{MW} and C-dots$^{MW}_{sonicated}$; and the XPS C 1s spectra of (d) C-dots^{MW} and (e) C-dots$^{MW}_{sonicated}$.

https://doi.org/10.1021/acsomega.1c00765
ACS Omega 2021, 6, 14174−14181

fluorophore ($\gamma \sim \zeta$) decreases (the relative area of each band is indicated in Table S1). The results support the consumption of molecular fluorophores and the growth of the carbon core. In Figure 3a, we have compared the Hg^{2+} ion sensitivity of C-dots^{MW} and C-dots$^{MW}_{sonicated}$. In the presence of Hg^{2+} ions, the emission of C-dots^{MW} is drastically quenched. Because the fluorescence quenching caused by Hg^{2+} only occurs at pH > 4.65, the binding of Hg^{2+} ion is associated with the presence of carboxylate groups (Figure S3). After sonication, the Stern–Volmer plot shows that C-dots^{MW} lose their Hg^{2+} ion sensitivity due to the loss of carboxylate groups, and we observed similar phenomena for the Cu^{2+} and Fe^{3+} ions (Figures S4 and S5). Moreover, when C-dots were mixed with a dioctyl sodium sulfosuccinate (AOT) (0.1%) + $AgNO_3$ (final concentration = 6 mM) solution and exposed to light-emitting diode (LED) light (color temperature = 5800 K and power = 4 mW/cm^2), the formation of the characteristic absorption band at 430 nm (Figure 3b,c) indicated that Ag^+ ions are photoreduced and formed Ag nanoparticles in the solution. Therefore, the time evolution of the absorbance at 430 nm can be used to evaluate the Ag^+ ion photoreduction activity of C-dots, and the results are indicated in the inset. In contrast to C-dots^{MW}, C-dots$^{MW}_{sonicated}$ show lower Ag^+ photoreduction activity, which suggests that C-dots^{MW} are oxidized after sonication, and the result is in agreement with the FT-IR and XPS studies. Another intriguing finding is that when the C-dot^{MW} solution was degassed using the freeze–pump–thaw method and sonicated (C-dots$^{MW\ anaerobic}_{sonicated}$), the Hg^{2+} ion sensitivity and the photoreduction activity were significantly higher than those of C-dots$^{MW}_{sonicated}$ (Figure S6). The results indicate that sonicating the C-dots^{MW} in an aerobic environment accelerates the oxidization of molecule-like fluorophores, which is harmful to the Φ_F, ion sensing, and photoreduction activities of C-dots^{MW}.

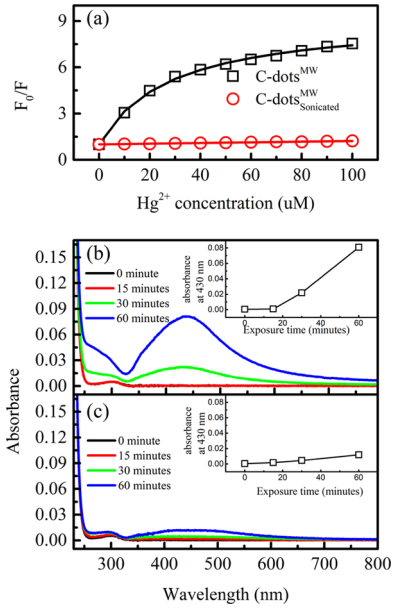

Figure 3. (a) Stern–Volmer plot of C-dots^{MW} and C-dots$^{MW}_{sonicated}$ titrated by Hg^{2+} ions. F_0 and F indicate the integrated fluorescence intensity (excitation wavelength = 350 nm) in the absence and prescence of Hg^{2+} ions, respectively.The absorption spectra of (b) C-dots^{MW} and (c) C-dots$^{MW}_{sonicated}$ mixed with AOT (0.1%) + $AgNO_3$ and exposed to a white-light LED. The insets indicate the time evolution of the absorbance at 430 nm.

Effects of the Hydrothermal Treatment on the Optical and Chemical Properties of C-Dots^{MW}. Figure 4a illustrates the steady-state spectra of the C-dots^{MW} autoclaved at 100 and 200 °C for 8 h. For the C-dots^{MW} autoclaved at 100 °C (C-dots$^{MW}_{100°C}$), the absorption spectrum closely resembles that of C-dots^{MW}, while the fluorescence quantum yield increases to 8.7%. For the C-dots^{MW} autoclaved at 200 °C (C-dots$^{MW}_{200°C}$), both the absorption and emission spectra were blue-shifted, and the fluorescence quantum yield increased to 15.8%. After the hydrothermal treatment, only C-dots$^{MW}_{200°C}$ exhibit EDF (Figure S7). In the fluorescence lifetime measurement (Figure 4b), the averaged fluorescence lifetimes of C-dots$^{MW}_{100°C}$ and C-dots$^{MW}_{200°C}$ were estimated to be 11.43 and 5.72 ns, respectively. In Table 1, we can see that the k_r of C-dots^{MW} increases drastically after the hydrothermal treatment and therefore leads to a shorter lifetime and higher Φ_f of C-dots$^{MW}_{100°C}$ and C-dots$^{MW}_{200°C}$. The change in the k_r and EDF of C-dots$^{MW}_{200°C}$ implies that the hydrothermal treatment at 200 °C may produce another kind of fluorophores. Although C-dots^{MW}, C-dots$^{MW}_{100°C}$, and C-dots$^{MW}_{200°C}$ exhibit similar size distributions in TEM images (Figure S8), C-dots$^{MW}_{200°C}$ exhibit much faster $r(t)$ than those of C-dot^{MW} and the C-dots$^{MW}_{100°C}$, and it can be fitted by single exponential decay with a time coefficient of 0.2 ns (Figure 4c). According to the size estimated from the TEM image, the rotational correlation time of C-dots$^{MW}_{200°C}$ should be about 0.66 ns, which is longer than the value we obtained. The discrepancy between the rotational correlation times estimated by $r(t)$ and TEM images suggested that the emission of C-dots$^{MW}_{200°C}$ was originated from the

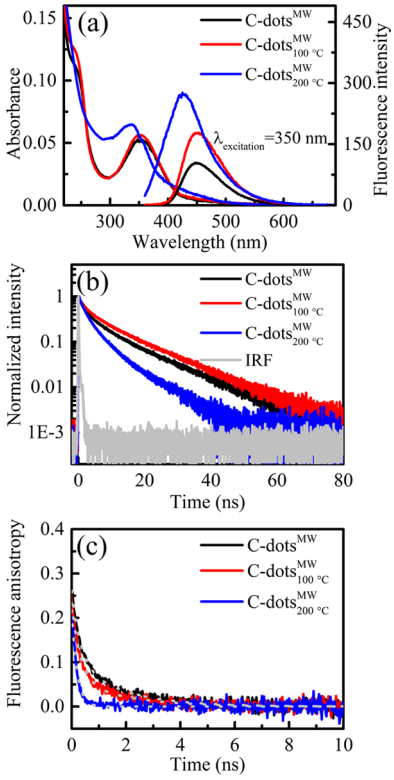

Figure 4. (a) Steady-state spectra, (b) fluorescence decay, and (c) fluorescence anisotropy decay dynamics of C-dots^{MW}, C-dots$^{MW}_{100°C}$, and C-dots$^{MW}_{200°C}$. The excitation wavelength was fixed at 375 nm.

https://doi.org/10.1021/acsomega.1c00765
ACS Omega 2021, 6, 14174–14181

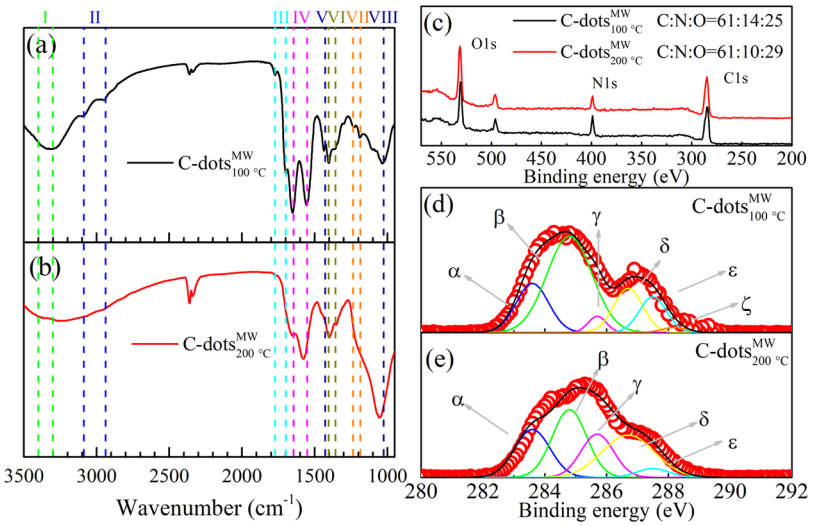

Figure 5. FT-IR spectra of (a) C-dots$^{MW}_{100°C}$ and (b) C-dots$^{MW}_{200°C}$; (c) the XPS survey scan of C-dots$^{MW}_{100°C}$ and C-dots$^{MW}_{200°C}$; and the XPS C 1s spectra of (d) C-dots $^{MW}_{100°C}$ and (e) C-dots$^{MW}_{200°C}$.

particles that are invisible in the TEM image. According to the previous studies, these particles are either encapsulated in the flexible region of C-dots[37] or suspended in the solution.[49] More importantly, the result indicates that the structures or types of fluorophores of C-dots are drastically changed during the hydrothermal process. This interpretation is further supported by nuclear magnetic resonance (NMR) studies. In which C-dots^{MW} and C-dots$^{MW}_{sonicated}$ exhibit broad polymer-like NMR patterns, while C-dots$^{MW}_{sonicated}$ show sharp NMR peaks after the hydrothermal treatment (Figure S9). Figure 5a,b shows the FT-IR spectra of C-dots$^{MW}_{100°C}$ and C-dots$^{MW}_{200°C}$, respectively. At a higher hydrothermal temperature, we observed a smaller vibrational band at 1774 cm^{-1}, and the signal at 1025 cm^{-1} increases significantly. The result indicates the loss of the carboxylic group and the oxidization of carbon dots during the hydrothermal process. In the XPS survey scan (Figure 5c), the composition of oxygen increases to 25 and 29% for C-dots$^{MW}_{100°C}$ and C-dots$^{MW}_{200°C}$, respectively. In the C 1s high-resolution spectra (Figure 5d,e), the integrated area of the C−O−C band increased, while the signal corresponding to the HO−C═O functional group decreased after the hydrothermal treatment (the relative area of each band is indicated in Table S1). Moreover, we also test the Hg^{2+} sensing and the photoreduction activity of C-dots^{MW} after the hydrothermal treatment. In Figure 6a, it is surprising that the emission of C-dots$^{MW}_{100°C}$ still shows the response to Hg^{2+} ions, and the Hg^{2+} ion sensitivity decreases in the following order C-dots^{MW} > C-dots$^{MW}_{100°C}$ > C-dots$^{MW}_{200°C}$. In Figure 6b, neither C-dots$^{MW}_{100°C}$ nor C-dots$^{MW}_{200°C}$ can be used to reduce the Ag^{+} ions via the photoreduction mechanism (Figure S10), which indicates that C-dots^{MW} lose their photoreduction activity after the hydrothermal treatment.

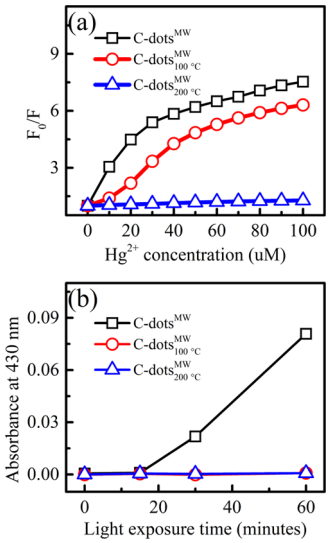

Figure 6. (a) Stern−Volmer plot of C-dots^{MW}, C-dots$^{MW}_{100°C}$, and C-dots$^{MW}_{200°C}$ titrated by Hg^{2+} ions. F_0 and F indicate the integrated fluorescence intensity (excitation wavelength = 350 nm) in the absence and prescence of Hg^{2+} ions, respectively. (b) Time evolution of the absorbance at 430 nm when C-dots^{MW}, C-dots$^{MW}_{100°C}$, and C-dots$^{MW}_{200°C}$ were mixed with AOT (0.1%) + $AgNO_3$ and exposed to a white-light LED.

CONCLUSIONS

In the current study, we have investigated the changes in the properties of C-dots^{MW} after sonication and hydrothermal treatments. The results indicated that sonicating the C-dots^{MW} in the aerobic condition significantly lowers their Φ_f, ion sensing, and photoreduction activity. The FT-IR and XPS studies indicate that the sonication process consumes the molecule-like fluorophores by accelerating the oxidization of surface functional groups. Therefore, the presence of oxygen is deleterious to the preservation of C-dots^{MW}. After the hydrothermal treatment, the FT-IR, XPS, and NMR studies suggested that the molecular fluorophores attached to C-dots^{MW} can further react and generate new fluorophores with higher Φ_f. The Hg^{2+} sensing and photoreduction activity tests show that C-dots$^{MW}_{200°C}$ lose their Hg^{2+} ion sensitivity and photoreduction activity due to the oxidization of surface functional groups. By autoclaving the C-dots^{MW} at 100 °C, we can improve the Φ_f of C-dots^{MW} without losing their Hg^{2+} ion sensitivity, The result also confirmed our hypothesis that C-dots^{MW} are still at the initial stage of pyrolysis or the carbonization process, and their properties could be improved by autoclaving at a mild temperature, which is beneficial to their application in ion-sensing studies.

https://doi.org/10.1021/acsomega.1c00765
ACS Omega 2021, 6, 14174−14181

EXPERIMENTAL SECTION

Materials and Preparation of C-Dots. Citric acid (≥99.5%, Sigma-Aldrich), ethylenediamine (99%, Alfa Aesar), quinine sulfate (>99.0%, Alfa Aesar), sulfuric acid (95−98%, J.T. Baker), silver nitrate (≥99.5%, Sigma-Aldrich), dioctyl sodium sulfosuccinate (AOT, ≥99.0%, Sigma), mercury chloride (≥99.5%, Sigma-Aldrich), copper chloride (99%, Sigma-Aldrich), iron chloride hexahydrate (98%, Sigma-Aldrich), and hydrochloric acid (>36.0%, J.T. Baker) were used as received, and deionized water (resistivity >18.2 MΩ) was prepared using Barnstead EasyPure II water purification system. For the preparation of C-dots, 0.423 g of citric acid and 0.360 g of ethylenediamine were dissolved in 10 mL of deionized water and microwaved using a domestic microwave oven (Sampo, RE-B320PM; power = 700 W) for 7 min. After cooling down to room temperature, the sample was dissolved in 5 mL of deionized water. The stock solution was filtered through a filter paper (pore size = 5 μm) and a syringe filter (pore size = 0.2 μm) to remove large particles. The filtered solution was further dialyzed (molecular weight cutoff (MWCO) = 50 kDa) against deionized water until the fluorescence signal of dialysate was less than 0.01% of the retentate solution (usually 5 days).

Characterization of C-Dots. The UV−vis absorption and fluorescence spectra were recorded using a Cary 100 UV−vis spectrophotometer and a Cary Eclipse fluorescence spectrophotometer, respectively. The fluorescence quantum yield (Φ_f) was determined using a 0.1 M H_2SO_4 solution as a reference (Φ_f = 0.54). For each sample, the absorbance at 350 nm was controlled at values <0.05, and the absorption and emission spectra were recorded at eight different concentrations. The slope (m) obtained from the plot of integrated fluorescence versus the absorbance at the excitation wavelength (which is 350 nm in our case) was used to calculate the fluorescence quantum yield using the following equation

$$\Phi_{sample} = \Phi_{standard}\left(\frac{m_{sample}}{m_{standard}}\right)\left(\frac{n^2_{sample}}{n^2_{standard}}\right) \quad (5)$$

where Φ and n denote the fluorescence quantum yield and the refractive index of the solvent, respectively. The Fourier transform infrared (FT-IR) spectra were recorded using a Bruker Tensor 27 FT-IR spectrometer, while the transmission electron microscopy (TEM) images were taken with a Hitachi HT7700 TEM. The X-ray photoelectron spectra (XPS) were obtained using a ULVAC-PHI, PHI 5000 VersaProbe. The NMR spectra were recorded using a Bruker Avance 300 MHz NMR spectrometer. The time-resolved fluorescence spectra were recorded using a home-build time-correlated single-photon counting system equipped with a PDL 800-D pulsed diode laser driver (Picoquant) and a TimeHarp 260 photon counting module (PicoQuant). The excitation light source was provided by a 375 nm pulsed diode laser (LDH-P-C-375 B). The sample was loaded in a 1 cm quartz cuvette and the emission was collected at the right angle position (relative to the excitation light). The fluorescence wavelength was selected by a monochromator and the signal was probed by a photomultiplier detector (PicoQuant, PMA 175). Two linear polarizers were used to control the polarization of the excitation light and fluorescence. The fluorescence decay dynamics was measured at the magic angle condition and deconvoluted using FluoFit software (PicoQuant). For the Hg^{2+} ion-sensing experiment, C-dot solutions were titrated with a 6 mM $HgCl_2$ solution. At each Hg^{2+} concentration, the samples were mixed with the $HgCl_2$ solution for at least 30 min and loaded in a 3 mm quartz cuvette for fluorescence measurement. For the photoreduction experiment, the C-dot solution was mixed with AOT (0.1%) and $AgNO_3$ (final concentration = 6 mM). The solution was exposed to LED light (color temperature = 5800 K and power = 4 mW/cm^2). To measure the change in the UV−vis spectra, the solutions were loaded in a 1 mm quartz cuvette.

ASSOCIATED CONTENT

Supporting Information

The Supporting Information is available free of charge at https://pubs.acs.org/doi/10.1021/acsomega.1c00765.

TEM images of C-dots^{MW} and C-dots$^{MW}_{sonicated}$ (Figure S1); emission spectra and emission peaks of C-dots^{MW} and C-dots$^{MW}_{sonicated}$ excited at different wavelengths (Figure S2); Hg^{2+} ion sensing at different pH values (Figure S3); Cu^{2+} sensing (Figure S4); Fe^{3+} sensing of C-dots (Figure S5); fluorescence quenching curve and absorbance changes at 430 nm of C-dots$^{MW\ anaerobic}_{sonicated}$ (Figure S6); fluorescence contour maps and emission peaks of C-dots^{MW} autoclaved at different temperatures (Figure S7); TEM image of C-dots^{MW} autoclaved at different temperatures (Figure S8); ^{1}H NMR spectra of C-dots (Figure S9); photoreduction experiments of C-dots$^{MW}_{100°C}$ and C-dots$^{MW}_{200°C}$ (Figure S10); and relative area of each deconvoluted XPS band (Table S1) (PDF)

AUTHOR INFORMATION

Corresponding Author

Chih-Wei Chang − *Department of Chemistry, National Changhua University of Education, Changhua City 50058, Taiwan;* orcid.org/0000-0002-8018-2312; Email: cwchang@cc.ncue.edu.tw

Authors

I-Hua Tsai − *Department of Chemistry, National Changhua University of Education, Changhua City 50058, Taiwan*

Jyun-Ting Li − *Department of Chemistry, National Changhua University of Education, Changhua City 50058, Taiwan*

Complete contact information is available at: https://pubs.acs.org/10.1021/acsomega.1c00765

Author Contributions

C.-W.C. designed the experiment and wrote the manuscript. I-H.T. and J.T.L. conducted the experiments.

Funding

MOST 109-2113-M-018-008.

Notes

The authors declare no competing financial interest.

ACKNOWLEDGMENTS

The authors appreciate the financial support from the Ministry of Science of Technology, Taiwan (project contract: MOST 108-2113-M-018-002). The authors also thank Prof. Li-Kang Chu (National Tsing-Hua University, Taiwan) for the FT-IR spectroscopy experiments.

REFERENCES

(1) Xu, X.; Ray, R.; Gu, Y.; Ploehn, H. J.; Gearheart, L.; Raker, K.; Scrivens, W. A. Electrophoretic Analysis and Purification of Fluorescent Single-Walled Carbon Nanotube Fragments. *J. Am. Chem. Soc.* **2004**, *126*, 12736−12737.

(2) Dong, Y.; Li, G.; Zhou, N.; Wang, R.; Chi, Y.; Chen, G. Graphene Quantum Dot as a Green and Facile Sensor for Free Chlorine in Drinking Water. *Anal. Chem.* **2012**, *84*, 8378−82.

(3) Zhang, R.; Chen, W. Nitrogen-Doped Carbon Quantum Dots: Facile Synthesis and Application as a "Turn-Off" Fluorescent Probe for Detection of Hg2+ Ions. *Biosens. Bioelectron.* **2014**, *55*, 83−90.

(4) Wang, C.; Jiang, K.; Xu, Z.; Lin, H.; Zhang, C. Glutathione Modified Carbon-Dots: From Aggregation-Induced Emission Enhancement Properties to a "Turn-on" Sensing of Temperature/Fe3+ Ions in Cells. *Inorg. Chem. Front.* **2016**, *3*, 514−522.

(5) Bui, T. T.; Park, S.-Y. A Carbon Dot−Hemoglobin Complex-Based Biosensor for Cholesterol Detection. *Green Chem.* **2016**, *18*, 4245−4253.

(6) Sri, S.; Kumar, R.; Panda, A. K.; Solanki, P. R. Highly Biocompatible, Fluorescence, and Zwitterionic Carbon Dots as a Novel Approach for Bioimaging Applications in Cancerous Cells. *ACS Appl. Mater. Interfaces* **2018**, *10*, 37835−37845.

(7) Pan, L.; Sun, S.; Zhang, L.; Jiang, K.; Lin, H. Near-Infrared Emissive Carbon Dots for Two-Photon Fluorescence Bioimaging. *Nanoscale* **2016**, *8*, 17350−17356.

(8) Jiang, K.; Sun, S.; Zhang, L.; Lu, Y.; Wu, A.; Cai, C.; Lin, H. Red, Green, and Blue Luminescence by Carbon Dots: Full-Color Emission Tuning and Multicolor Cellular Imaging. *Angew. Chem., Int. Ed.* **2015**, *54*, 5360−3.

(9) Wei, X.; Li, L.; Liu, J.; Yu, L.; Li, H.; Cheng, F.; Yi, X.; He, J.; Li, B. Green Synthesis of Fluorescent Carbon Dots from Gynostemma for Bioimaging and Antioxidant in Zebrafish. *ACS Appl. Mater. Interfaces* **2019**, *11*, 9832−9840.

(10) Li, H.; Yan, X.; Qiao, S.; Lu, G.; Su, X. Yellow-Emissive Carbon Dot-Based Optical Sensing Platforms: Cell Imaging and Analytical Applications for Biocatalytic Reactions. *ACS Appl. Mater. Interfaces* **2018**, *10*, 7737−7744.

(11) Zhu, S.; Zhang, J.; Qiao, C.; Tang, S.; Li, Y.; Yuan, W.; Li, B.; Tian, L.; Liu, F.; Hu, R.; Gao, H.; Wei, H.; Zhang, H.; Sun, H.; Yang, B.; et al. Strongly Green-Photoluminescent Graphene Quantum Dots for Bioimaging Applications. *Chem. Commun.* **2011**, *47*, 6858−60.

(12) Cailotto, S.; Mazzaro, R.; Enrichi, F.; Vomiero, A.; Selva, M.; Cattaruzza, E.; Cristofori, D.; Amadio, E.; Perosa, A. Design of Carbon Dots for Metal-Free Photoredox Catalysis. *ACS Appl. Mater. Interfaces* **2018**, *10*, 40560−40567.

(13) Martins, N. C. T.; Ângelo, J.; Girão, A. V.; Trindade, T.; Andrade, L.; Mendes, A. N-Doped Carbon Quantum Dots/Tio2 Composite with Improved Photocatalytic Activity. *Appl. Catal., B* **2016**, *193*, 67−74.

(14) Mehta, A.; D, P.; Thakur, A.; Basu, S. Enhanced Photocatalytic Water Splitting by Gold Carbon Dot Core Shell Nanocatalyst under Visible/Sunlight. *New J. Chem.* **2017**, *41*, 4573−4581.

(15) Li, H.; Kong, W.; Liu, J.; Yang, M.; Huang, H.; Liu, Y.; Kang, Z. Carbon Dots for Photoswitching Enzyme Catalytic Activity. *J. Mater. Chem. B* **2014**, *2*, 5652−5658.

(16) Wang, Y. L.; Zhao, Y. Q.; Zhang, Y.; Zhang, F.; Feng, X. T.; Chen, L.; Yang, Y. Z.; Liu, X. G. A Single-Phase Heteroatom Doped Carbon Dot Phosphor toward White Light-Emitting Diodes. *RSC Adv.* **2016**, *6*, 38761−38768.

(17) Hu, T.; Wen, Z.; Wang, C.; Thomas, T.; Wang, C.; Song, Q.; Yang, M. Temperature-Controlled Spectral Tuning of Full-Color Carbon Dots and Their Strongly Fluorescent Solid-State Polymer Composites for Light-Emitting Diodes. *Nanoscale Adv.* **2019**, *1*, 1413−1420.

(18) Guo, X.; Wang, C.-F.; Yu, Z.-Y.; Chen, L.; Chen, S. Facile Acess to Versatile Fluorescent Carbon Dots toward Light-Emitting Diodes. *Chem. Commun.* **2012**, *48*, 2692−2694.

(19) Zhu, S.; Song, Y.; Zhao, X.; Shao, J.; Zhang, J.; Yang, B. The Photoluminescence Mechanism in Carbon Dots (Graphene Quantum Dots, Carbon Nanodots, and Polymer Dots): Current State and Future Perspective. *Nano Res.* **2015**, *8*, 355−381.

(20) Lim, S. Y.; Shen, W.; Gao, Z. Carbon Quantum Dots and Their Applications. *Chem. Soc. Rev.* **2015**, *44*, 362−381.

(21) Wang, K.; Gao, Z.; Gao, G.; Wo, Y.; Wang, Y.; Shen, Gx.; Cui, D. Systematic Safety Evaluation on Photoluminescent Carbon Dots. *Nanoscale Res. Lett.* **2013**, *8*, No. 122.

(22) Geng, B.; Yang, D.; Pan, D.; Wang, L.; Zheng, F.; Shen, W.; Zhang, C.; Li, X. Nir-Responsive Carbon Dots for Efficient Photothermal Cancer Therapy at Low Power Densities. *Carbon* **2018**, *134*, 153−162.

(23) Zhou, B.; Guo, Z.; Lin, Z.; Zhang, L.; Jiang, B.-P.; Shen, X.-C. Recent Insights into near-Infrared Light-Responsive Carbon Dots for Bioimaging and Cancer Phototherapy. *Inorg. Chem. Front.* **2019**, *6*, 1116−1128.

(24) Zheng, M.; Li, Y.; Liu, S.; Wang, W.; Xie, Z.; Jing, X. One-Pot to Synthesize Multifunctional Carbon Dots for near Infrared Fluorescence Imaging and Photothermal Cancer Therapy. *ACS Appl. Mater. Interfaces* **2016**, *8*, 23533−23541.

(25) Xu, X.; Bao, Z.; Zhou, G.; Zeng, H.; Hu, J. Enriching Photoelectrons Via Three Transition Channels in Amino-Conjugated Carbon Quantum Dots to Boost Photocatalytic Hydrogen Generation. *ACS Appl. Mater. Interfaces* **2016**, *8*, 14118−14124.

(26) Qian, X.; Yue, D.; Tian, Z.; Reng, M.; Zhu, Y.; Kan, M.; Zhang, T.; Zhao, Y. Carbon Quantum Dots Decorated Bi2wo6 Nanocomposite with Enhanced Photocatalytic Oxidation Activity for Vocs. *Appl. Catal., B* **2016**, *193*, 16−21.

(27) Zhang, H.; Liu, J.; Wang, B.; Liu, K.; Chen, G.; Yu, X.; Li, J.; Yu, J. Zeolite-Confined Carbon Dots:Tuning Thermally Activated Delayed Fluorescence Emission Via Energy Transfer. *Mater. Chem. Fron* **2020**, *4*, 1404−1410.

(28) Yang, T.; Dai, S.; Yang, S.; Chen, L.; Liu, P.; Dong, K.; Zhou, J.; Chen, Y.; Pan, H.; Zhang, S.; et al. Interfacial Clustering-Triggered Fluorescence-Phosphorescence Dual Solvoluminescence of Metal Nanoclusters. *J. Phys. Chem. Lett.* **2017**, *8*, 3980−3985.

(29) Wang, C.; Chen, Y.; Hu, T.; Chang, Y.; Ran, G.; Wang, M.; Song, Q. Color Tunable Room Temperature Phosphorescent Carbon Dots Based Nanocomposites Obtainable from Multiple Carbon Source Via a Molten Salt Method. *Nanoscale* **2019**, *11*, 11967−11974.

(30) Gou, H.; Liu, Y.; Zhang, G.; Liao, Q.; Huang, X.; Ning, F.; Ke, C.; Meng, Z.; Xi, K. Lifetime-Tunable Room-Temperature Phosphorescence of Polyaniline Carbon Dots in Adjustable Polymer Matrices. *Nanoscale* **2019**, *11*, 18311−18319.

(31) Kim, S.; et al. Anomalous Behaviors of Visible Luminescence from Graphene Quantum Dots: Interplay between Size and Shape. *ACS Nano* **2012**, *6*, 8203−8208.

(32) Manioudakis, J.; Victoria, F.; Thompson, C. A.; Brown, L.; Movsum, M.; Lucifero, R.; Naccache, R. Effects of Nitrogen-Doping on the Photophysical Properties of Carbon Dots. *J. Mater. Chem. C* **2019**, *7*, 853−862.

(33) Liu, X.; Li, H.-B.; Shi, L.; Meng, X.; Wang, Y.; Chen, X.; Xu, H.; Zhang, W.; Fang, X.; Ding, T. Structure and Photoluminescence Evolution of Nanodots During Pyrolysis of Citric Acid: From Molecular Clusters to Carbogenic Nanoparticles. *J. Mater. Chem. C* **2017**, *5*, 10302−10312.

(34) Fang, Q.; Dong, Y.; Chen, Y.; Lu, C.-H.; Chi, Y.; Yang, H.-H.; Yu, T. Luminescence Origin of Carbon Based Dots Obtained from Citric Acid and Amino Group Containing Molecules. *Carbon* **2017**, *118*, 319−326.

(35) Zhu, S.; Zhao, X.; Song, Y.; Lu, S.; Yang, B. Beyond Bottom-up Carbon Nanodots: Citric-Acid Derived Organic Molecules. *Nano Today* **2016**, *11*, 128−132.

(36) Das, A.; Gude, V.; Roy, D.; Chatterjee, T.; De, C. K.; Mandal, P. K. On the Molecular Origin of Photoluminescence of Nonblinking Carbon Dot. *J. Phys. Chem. C* **2017**, *121*, 9634−9641.

(37) Das, A.; Roy, D.; De, C. K.; Mandal, P. K. "Where Does the Fluorescing Moiety Reside in a Carbon Dot?"-Investigations Based on Fluorescence Anisotropy Decay and Resonance Energy Transfer Dynamics. *Phys. Chem. Chem. Phys.* **2018**, *20*, 2251−2259.

https://doi.org/10.1021/acsomega.1c00765
ACS Omega 2021, 6, 14174−14181

(38) Krysmann, M. J.; Kelarakis, A.; Dallas, P.; Giannelis, E. P. Formation Mechanism of Carbogenic Nanoparticles with Dual Photoluminescence Emission. *J. Am. Chem. Soc.* **2012**, *134*, 747−750.
(39) Qu, D.; Sun, Z. The Formation Mechanism and Fluorophores of Carbon Dots Synthesized Via a Bottom-up Route. *Mater. Chem. Front.* **2020**, *4*, 400−420.
(40) Song, Y.; Zhu, S.; Zhang, S.; Fu, Y.; Wang, L.; Zhao, X.; Yang, B. Investigation from Chemical Structure to Photoluminescent Mechanism: A Type of Carbon Dots from the Pyrolysis of Citric Acid and an Amine. *J. Mater. Chem. C* **2015**, *3*, 5976−5984.
(41) Lakowicz, J. R. *Principles of Fluorescence Spectroscopy*; 3rd ed.; Springer, 2006.
(42) Dhenadhayalan, N.; Lin, K.-C.; Suresh, R.; Ramamurthy, P. Unravelling the Multiple Emissive States in Citric-Acid-Derived Carbon Dots. *J. Phys. Chem. C* **2016**, *120*, 1252−1261.
(43) Vallan, L.; Urriolabeitia, E. P.; Ruipérez, F.; Matxain, J. M.; Canton-Vitoria, R.; Tagmatarchis, N.; Benito, A. M.; Maser, W. K. Supramolecular-Enhanced Charge Transfer within Entangled Polyamide Chains as the Origin of the Universal Blue Fluorescence of Polymer Carbon Dots. *J. Am. Chem. Soc.* **2018**, *140*, 12862−12869.
(44) Irfan, M.; Bhat, S. I.; Ahmad, S. Waterborne Reduced Graphene Oxide Dispersed Bio-Polyesteramide Nanocomposites: An Approach Towards Eco-Friendly Anticorrosive Coatings. *New. J. Chem.* **2019**, *43*, 4706−4720.
(45) Cai, K.; Zuo, S.; Luo, S.; Yao, C.; Liu, W.; Ma, J.; Mao, H.; Li, Z. Preparation of Polyaniline/Graphene Composites with Excellent Anti-Corrosion Properties and Their Application in Waterborne Polyurethane Anticorrosive Coatings. *RSC Adv.* **2016**, *6*, 95965−95972.
(46) Siddique, A. B.; Pramanick, A. K.; Chatterjee, S.; Ray, M. Amorphous Carbon Dots and Their Remarkable Ability to Detect 2,4,6-Trinitrophenol. *Sci. Rep.* **2018**, *8*, No. 9770.
(47) Ganesan, K.; Ghosh, S.; Krishna, N. G.; llango, S.; Kamruddin, M.; Tyagi, A. K. A Comparative Study on Defect Estimation Using Xps and Raman Spectroscopy in Few Layer Nanographitic Structures. *Phys. Chem. Chem. Phys.* **2016**, *18*, 22160−22167.
(48) Rabchinskii, M. K.; Dideikin, A. T.; Kirilenko, D. A.; Baidakova, M. V.; Shnitov, V. V.; Roth, F.; Konyakhin, S. V.; Besedina, N. A.; Pavlov, S. I.; Kuricyn, R. A.; et al. Facile Reduction of Graphene Oxide Suspensions and Films Using Glass Wafers. *Sci. Rep.* **2018**, *8*, No. 14154.
(49) Hsu, Y.-F.; Chen, Y.-H.; Chang, C.-W. The Spectral Heterogeneity and Size Distribution of the Carbon Dots Derived from Time-Resolved Fluorescence Studies. *Phys. Chem. Chem. Phys.* **2016**, *18*, 30086−30092.

https://doi.org/10.1021/acsomega.1c00765
ACS Omega 2021, 6, 14174−14181